Electronic Supplementary Information

Magnetism-induced diffuse scattering effect trigging excellent thermoelectric performance

*Wei Song[1], Chuanqing Sun[1], Kangkang Yang[1], Shaoqiu Ke[1], Xiangyu Li[1], Mingrui Liu[3], Congli Sun[1,2] *, Wenyu Zhao[1,3] *, Qingjie Zhang[1]*

[1]State Key Laboratory of Advanced Technology for Materials Synthesis and Processing, International School of Materials Science and Engineering, Wuhan University of Technology, Wuhan 430070, China

[2]NRC (Nanostructure Research Centre), Wuhan University of Technology, Wuhan 430070, China

[3]Foshan Xianhu Laboratory of the Advanced Energy Science and Technology Guangdong Laboratory, Xianhu, 528000, China

*Corresponding authors (e-mail: wyzhao@whut.edu.cn; conglisun@whut.edu.cn)

S1. Section morphology analysis from FESEM

The field emission scanning electron microscope (FESEM) was carried out on the fresh fracture section of all the samples (**Fig. S1**). Each sample shows a rather compact morphology with no obvious cracks. The images confirm the presence of Co particles in the composites without localized aggregation.
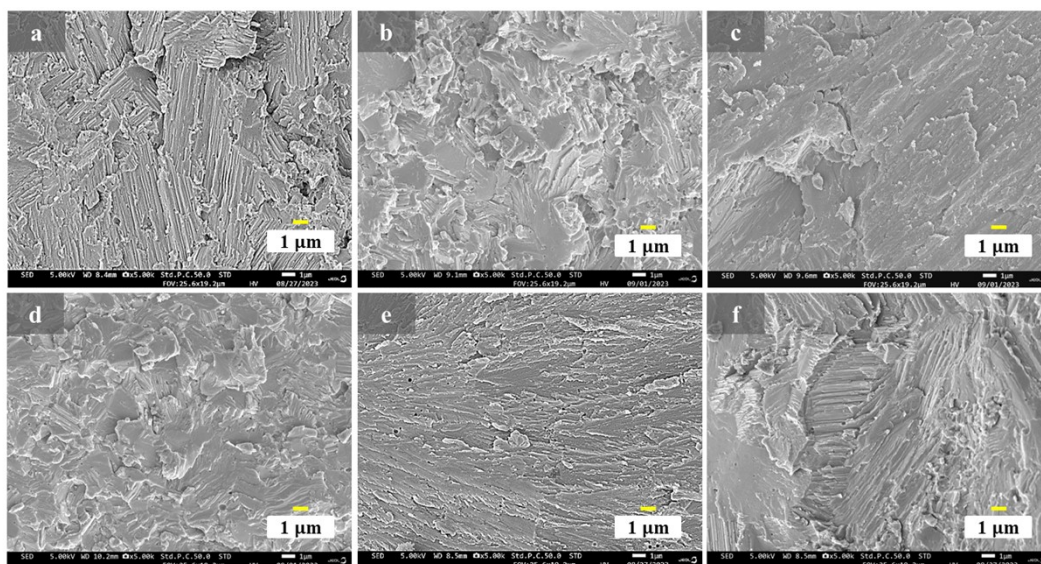

Fig. S1 | SEM-BSE micrographs of xCo/Mg$_{3.2}$Bi$_{1.49}$Sb$_{0.5}$Te$_{0.01}$ (x=0, 0.005, 0.01, 0.02, 0.03 and 0.04) compositions. (**a-f**) SEM-BSE micrographs for Co00, Co005, Co01, Co02, Co03 and Co04, respectively.

S2-S5. Mapping of composition elements from EPMA analysis

To further investigate the element distribution, the electron probe microanalyzer (EPMA) was performed with wavelength dispersive spectroscopy (WDS) mapping in **Fig. S2-4**. It can be clearly observed that the elements (Mg, Sb, Bi, Te) were distributed almost uniformly. However, Co particles (Co-Ps) aggregated more significantly as increasing Co-Ps content, resulting in the increase of radius of the Co inclusions in **Fig. S5**. In order to clarify the situation of different contrast area, the element quantitative analysis will be carried out later in **Fig. S6-8**.
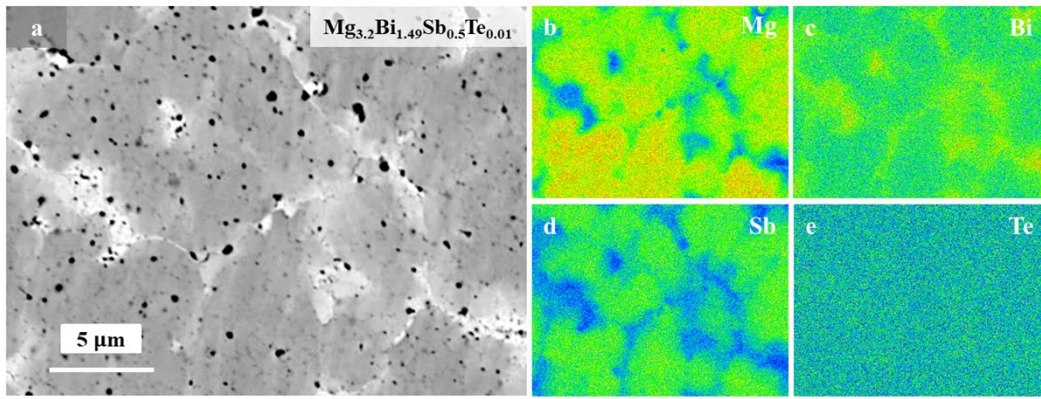
Fig. S2 | The surface microstructures of Co00. (a) the backscattered electron image and (**b-e**) the WDS mapping of Mg, Bi, Sb and Te elements.
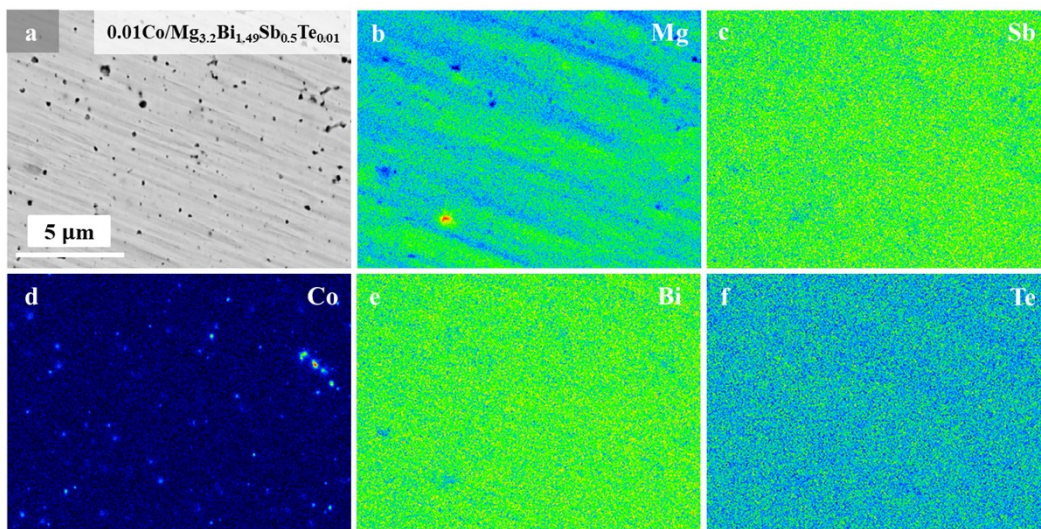

Fig. S3 | The surface microstructures of Co01. (a) the backscattered electron image and (**b-f**) the WDS mapping of Mg, Sb, Co, Bi and Te elements.
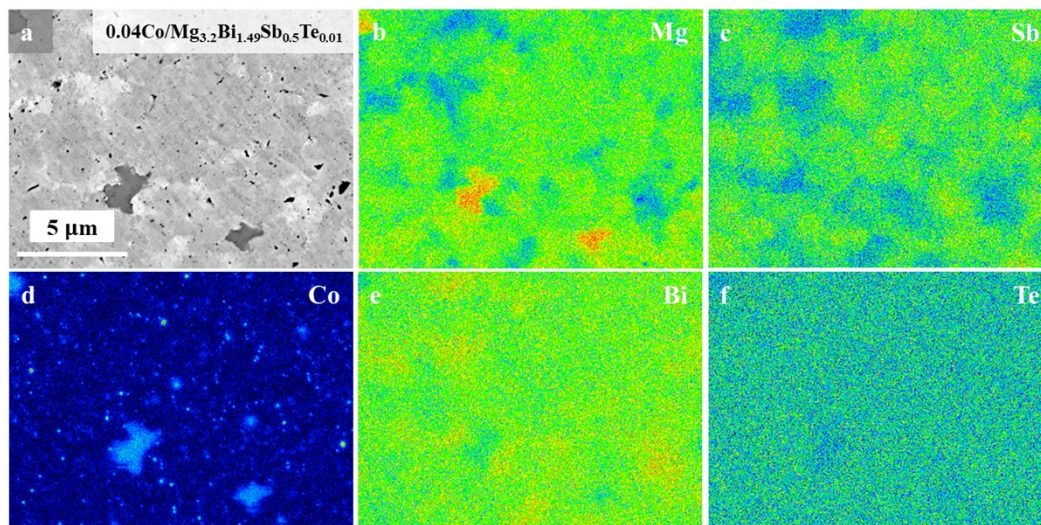

Fig. S4 | The surface microstructures of Co04. (a) the backscattered electron image and (**b-f**) the WDS mapping of Mg, Sb, Co, Bi and Te elements.
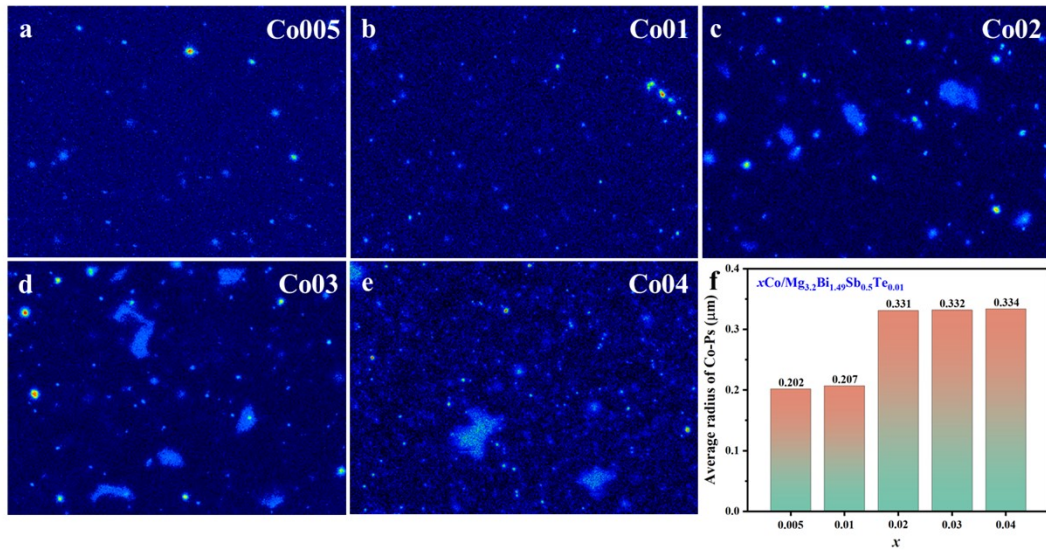
Fig. S5 | The surface microstructures of Co005-Co04. (a-e) the WDS mapping of Co elements for Co005, Co01, Co02, Co03 and Co04, respectively. **(f)** The increased radius of Co inclusions with increasing x.

S6-S8. Element quantitative analysis from EPMA analysis

Fig. S6a depicts the secondary electron image of Co00, and **Fig. S6b** depicts the backscattered electron image of Co00. **Fig. S7a** and **Fig. S8a** depict the secondary electron image of Co00 and Co04, respectively. **Fig. S7b** and **Fig. S8b** depict the backscattered electron image of Co00 and Co04, respectively. It can be clearly seen that the black contrast area corresponds to the hole area of the secondary electron image. In order to analyze the element distribution, EDS regional element analyses were conducted at the grey contrast (Red area), white contrast (Green area) and dark grey contrast (Blue area), respectively. The specific results are shown in **Table S1-3**. The Co content in the blue area is more than normal ratio. It is obvious that Co will aggregate in the dark grey contrast.
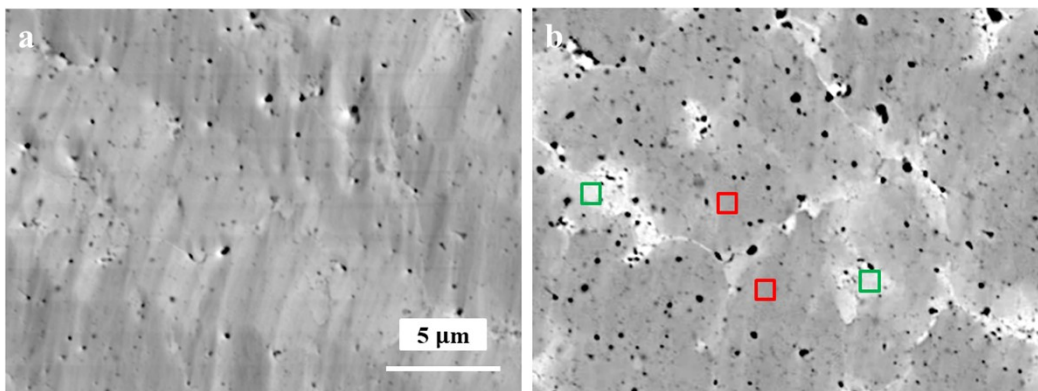
Fig. S6 | The surface microstructures of Co00. (a) the secondary electron image and **(b)** the backscattered electron image.

Table S1. EDS regional element analysis of Co00

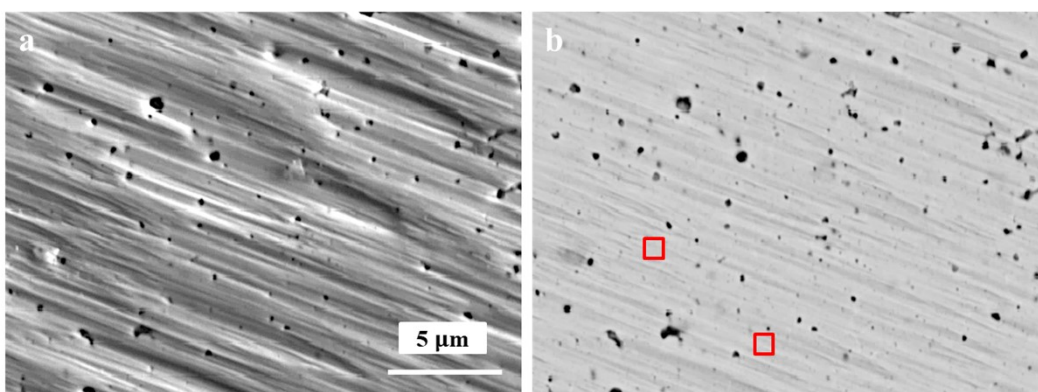| Area	Mg at.%	Bi at.%	Sb at.%	Te at.%
Red area	51.68	33.84	14.25	0.23
Green area	34.37	51.80	13.40	0.43

Fig. S7 | The surface microstructures of Co01. (a) the secondary electron image and **(b)** the backscattered electron image.

Table S2. EDS regional element analysis of Co01

Area	Mg	Bi	Sb	Te	Co

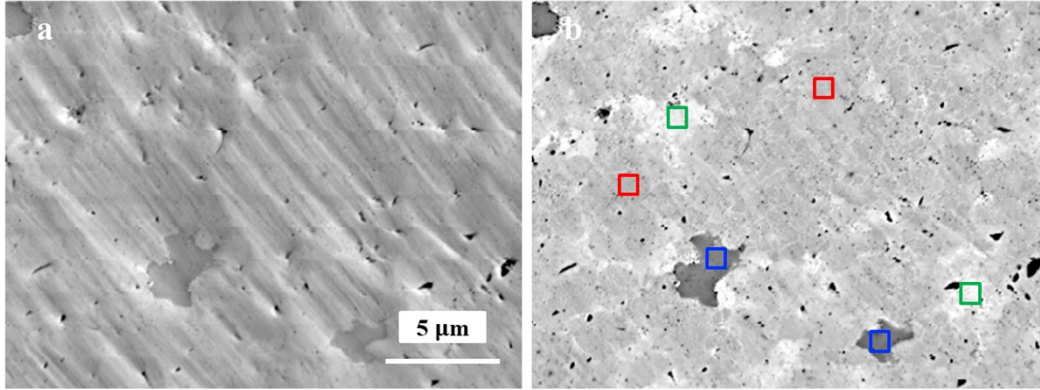|	at.%	at.%	at.%	at.%	at.%
Red area	55.43	33.37	10.85	0.18	0.17

Fig. S8 | The surface microstructures of Co04. (**a**) the secondary electron image and (**b**) the backscattered electron image.

Table S3. EDS regional element analysis of Co04

Area	Mg at.%	Bi at.%	Sb at.%	Te at.%	Co at.%
Red area	49.20	35.61	14.43	0.24	0.52
Green area	37.71	47.57	12.40	0.34	1.98
Blue area	40.65	33.84	14.51	0.19	10.81

S9. Room-temperature Raman spectrum analysis

To reveal the decreased lattice thermal conductivity, the Raman spectrum was examined in **Fig. 4c**. The Raman peaks at about 58.59 and 82.93 cm^{-1} correspond to the TO and LO modes of original Mg$_3$Sb$_2$, respectively[1]. To further investigate the accurate Raman frequencies and linewidths of TO mode, Raman spectrum with Lorentzian deconvolutions were shown in **Fig. S9**. The shift of TO mode to lower

frequencies indicates the reduction in sound velocity (v_s). It is known that the decreased v_s helps to reduce the κ_{L}[2]. Line broadening was characterized by Full Width at Half Maximum (FWHM). The FWHM of TO mode is 9.61 for Co00, whereas the FWHM of Co005, Co01, Co02, Co03 and Co04 samples are about 10.66, 12.45, 12.63, 13.54 and 14.24, respectively (**Table S4**). These results suggest that lattice disorder increases with Co-Ps addition. Due to the lattice mismatch induced by Mg_3Sb_2-Mg_3Bi_2 alloying, Mg vacancies (V_{Mg}^{2-}) generated by Mg volatilization during high-temperature sintering and the adding of magnetic Co-Ps introduces inhomogeneous strain and defect in Co0x samples. Therefore, the increased degree of lattice disorder from non-uniform strain leads to a line broadening by incorporating Co-Ps[3].

To further reveal the role of the lattice disorder in the thermal transport performance. The phonon lifetimes τ of the TO mode are calculated according to the following equation (2)[4]:

$$\frac{\Gamma}{\hbar} = \frac{1}{\tau} \#(1)$$

where Γ is the Raman linewidth in cm^{-1} and $\hbar = 5.3 \times 10^{-12}$ cm^{-1}s. The values of τ decrease with the increase of Γ, as shown in **Figure 4d** and **Table S4**. This indicates a strong phonon scattering in Co0x samples[5]. According to the above increased Γ and the decreased τ investigation, the increase of lattice disorder can suppress the phonon lifetime of Co0x samples. It is known that the phonon lifetime plays a key role in reducing κ_{L} in Mg_3Sb_2[6,7]. Therefore, it can be concluded that magnetic Co particles can help to reduce the RT κ_{L}.
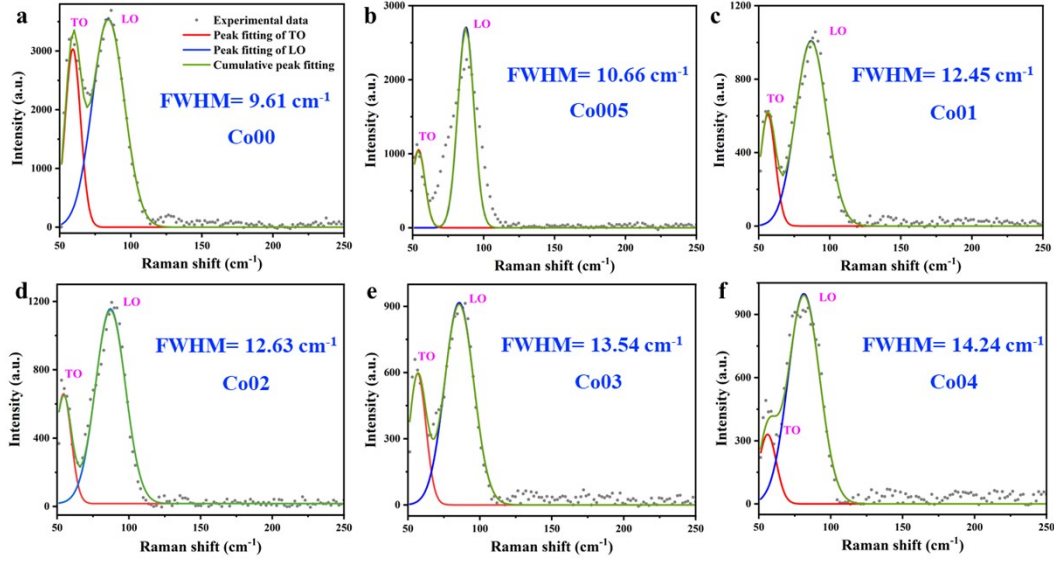
Fig. S9 | Room-temperature Raman spectrum with Lorentzian deconvolutions. (a-f) Room-temperature Raman spectrum with Lorentzian deconvolutions for Co00, Co005, Co01, Co02, Co03 and Co04 samples, respectively.

Table S4. Raman FWHM and phonon lifetime of samples

Samples	FWHM cm^{-1}	Phonon Lifetime ps
Co00	9.61	0.55
Co005	10.66	0.50
Co01	12.45	0.43
Co02	12.63	0.42
Co03	13.54	0.39
Co04	14.24	0.37

S10. Important parameters of electrical transport properties

Fig. S10a shows the temperature-dependent Hall coefficient R_H is negative over the complete temperature range, indicating n-type conduction. **Fig. S10b** shows the α

of the samples as a function of T. Over the entire temperature range of 300-800 K, the negative α shows a n-type conduction behavior. Due to the presence of negatively charged Mg vacancies (V_{Mg}^{2-}), $Mg_3(Sb,Bi)_2$ has been considered as persistent p-type TE materials. Therefore, it can be concluded that the formation of V_{Mg}^{2-} can be well suppressed in our experiments. As temperature increases, the α increases in the low temperature region and then decreases with elevating temperature, which reveals a thermally activated transport behavior. The Seebeck coefficient is inversely proportional to the carrier concentration n, or $n^{2/3}$, according to the Mott's relation,[8]

$$S = \left(\frac{8\pi^2 K_B^2}{3eh^2}\right) m^* T \left(\frac{\pi}{3n}\right)^{\frac{2}{3}} \#(2)$$

where, m^* is the effective mass, T is the absolute temperature, h is Planck's constant, e is electron charge and k_B is Boltzmann's constant. The RT Seebeck coefficient is increased from -140.84 $\mu V \cdot K^{-1}$ for Co00 to -155.86 $\mu V \cdot K^{-1}$ for Co01. However, the Hall effect measurement results did not show any decrement in the n (**Fig. 2c**). The scattering mechanism and carrier concentration have the dominated effect on the Seebeck coefficient.[9,10] These results indicate that the enhancement of Seebeck coefficient with x= 0.005 ~ 0.02 is initiated from the energy filtering effect (EFE). The dispersed Co-Ps formed incoherent interface boundaries between the matrix and Co-Ps. Such interfaces act as scattering centers that strengthen the EFE for charge carriers.[11,12] Only high-energy carriers can pass through the interface/boundary barrier. Hence, the enhanced energy filtering and carrier scattering mechanism caused the enhancement of the α at Co005 ~ Co02 samples. However, when Co-Ps tend to more significantly aggregate (x = 0.03 ~ 0.04), the EFE was suppressed and α was lower than the Co00.
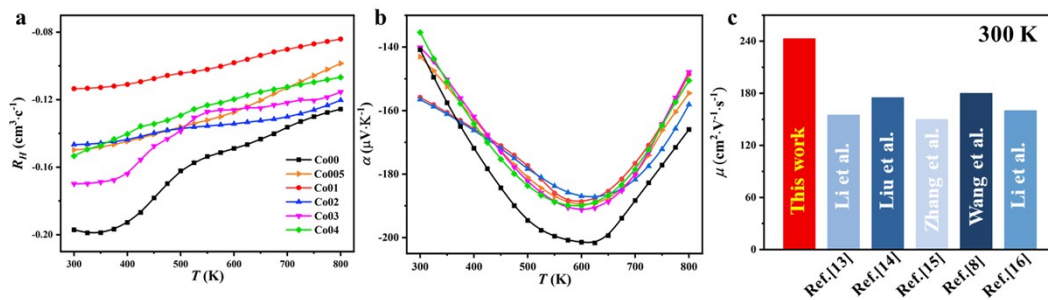

Fig. S10 | Electrical transport properties of the xCo/$Mg_{3.2}Bi_{1.49}Sb_{0.5}Te_{0.01}$ (x = 0,

0.005, 0.01, 0.02, 0.03 and 0.04) samples. Temperature dependent of (**a**) The Hall coefficient R_H, (**b**) Seebeck coefficient and (**c**) the comparison of the carrier mobility in this work with previously reported results.[8,13-16]

S11. Important parameters of thermal transport properties

Using the Wiedemann-Franz relationship, $\kappa_e = L\sigma T$, where L is the Lorentz number. The L for the materials with experimental Seebeck coefficient values can be calculated by the relation shown in equation (3):

$$L = 1.5 + exp\left[-\frac{|s|}{116}\right] \#(3)$$

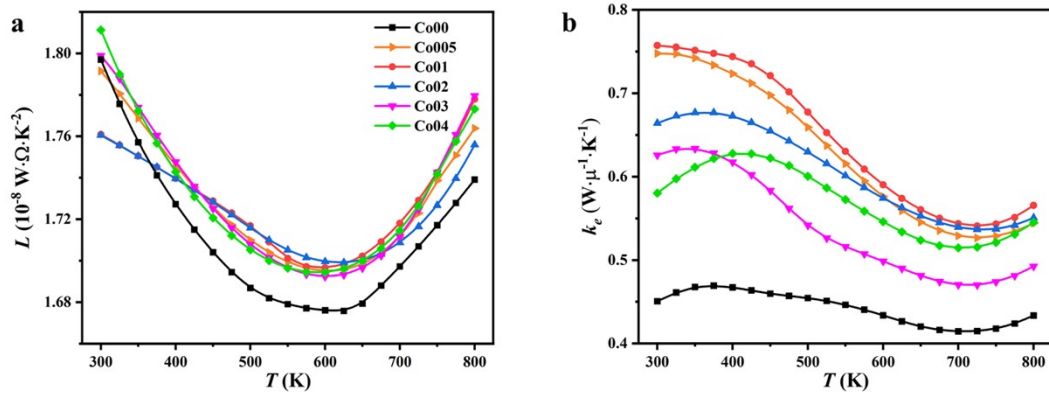The increased κ_e stems from the improvement of the σ in **Fig. 2b**.

Fig. S11 | Thermal transport properties of xCo/Mg$_{3.2}$Bi$_{1.49}$Sb$_{0.5}$Te$_{0.01}$ (x = 0, 0.005, 0.01, 0.02, 0.03 and 0.04) samples. Temperature dependent of (**a**) Lorentz number and (**b**) electronic thermal conductivity.

S12. The lattice parameters as a function of Co content.

The effective mass (m^*) is constant because Co atoms do not occupy the lattice sites and the lattice parameters remains almost unchanged.
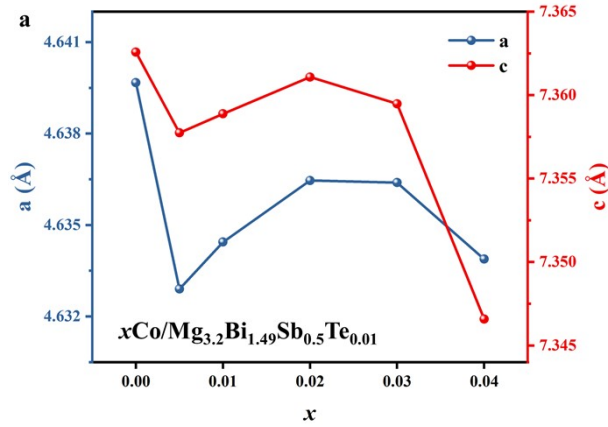
Fig. S12. (a) The lattice parameters as a function of Co content.

S13. The *NMR* at 100K

To further determine the observed *NMR* from WL effect and DS, the *NMR* for the Co0x samples at 100K were investigated for convenience. The actual *NMR* and fitting curves of two kinds of *NMR* are shown in **Fig. S13** with the color remarks and the dotted lines, respectively. The fitting curves of two kinds of *NMR* show good agreement to the actual *NMR*. As a result, the NMR_{WL} constant K_1 of Co005, Co01, Co02, Co03 and Co04 samples are 1.17, 1.44, 1.15, 0.91 and 0.65, respectively, whereas the corresponding NMR_{DS} constant K_2 are -0.16, -0.20, -0.15, -0.12 and -0.08, respectively. Therefore, *MR* theory can better reveal the scattering mechanism of the enhanced electrical performance.
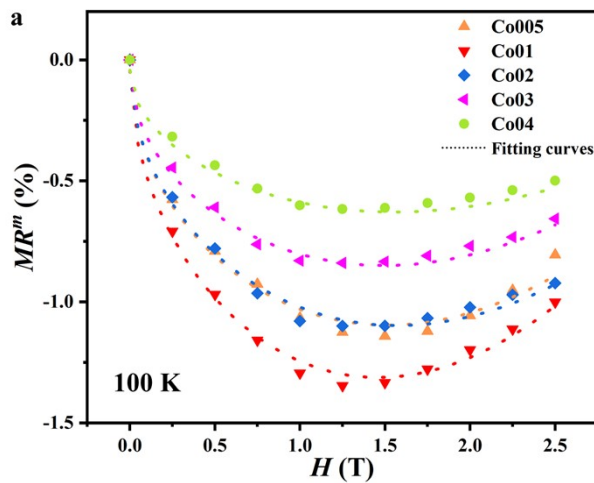

Fig. S13 | **(a)** The actual *NMR* and fitting curves of two kinds of *NMR* at 100 K of Co0x (x = 0.005, 0.01, 0.02, 0.03 and 0.04) samples with the color remarks and the dotted

lines, respectively.

S14-S16. Stability of thermoelectric Performance

In practical TE applications, in addition to having high TE properties, they also need to exhibit good thermal stability. The stability issues of $Mg_3(Sb,Bi)_2$-based materials, including Mg loss, oxidization and possible deterioration of TE performance at elevated temperature,[17] need to be well addressed. Previous reports suggest that the deterioration of TE performance is attributed to the Mg loss as well as the high reactivity of Mg atoms.[18,19] An approximately 11 wt.% of elemental bismuth crystallizing as a secondary phase in $Mg_3Sb_{1.475}Bi_{0.475}Te_{0.05}$ due to the unstable structure after the first thermal cycle.[20] Boron nitride coating on $Mg_3(Sb,Bi)_2$-based materials was confirmed as an effective solution to improve the thermal stability.[21] In this work, to further assess the thermal stability upon the addition of Co-Ps, the total nine thermal cycling tests were performed for the Co00 and Co0x samples (x = 0.01 and 0.02). It can be clearly seen that the RT σ of Co0x samples remains still above 80% after 9 thermal circles (**Fig. 8a**). In contrast, the RT σ of Co00 decreases quickly to 15% only after four thermal cycles. Simultaneously, the α and zT values of Co0x samples decrease rarely after 9 thermal circles (**Fig. 8b-c**). However, the RT α of Co00 becomes positive only after four thermal cycles, indicating the transition to inferior p-type conduction behavior. Due to the high reactivity and vapor pressure of Mg, severe Mg loss will occur with increasing thermal circles, which leads to the increase of the negatively charged Mg vacancies and eventually a transition to p-type conduction. In addition, the similar results at 350 K, 400 K and 450 K were shown in Fig. S14-16. In contrast, the Mg loss is inhibited by tuning its intrinsic migration kinetics after Co incorporation, which improves the structural stability by kinetically trapping the Mg framework[19]. Therefore, it can be concluded that incorporating Co-Ps is an effective method to improve the thermal stability in $Mg_3(Sb,Bi)_2$-based materials.

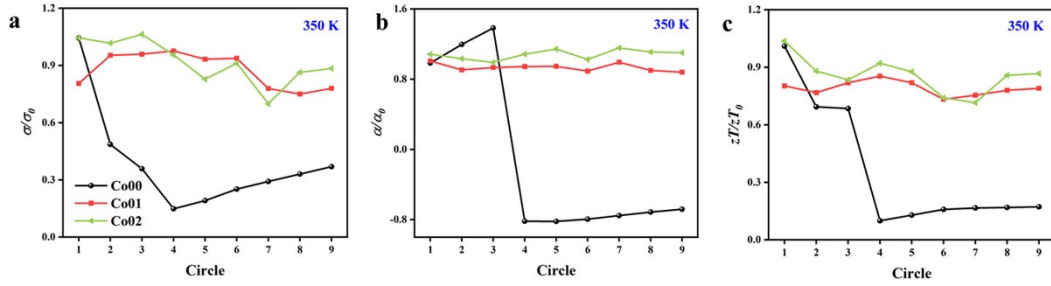**Fig. S14 | Stability performance of xCo/Mg$_{3.2}$Bi$_{1.49}$Sb$_{0.5}$Te$_{0.01}$ (x = 0, 0.01 and 0.02) at 350 K. (a)** σ/σ_0, **(b)** α/α_0 and **(c)** zT/zT_0. σ_0, α_0 and zT_0 are the corresponding values before the stability measurement.
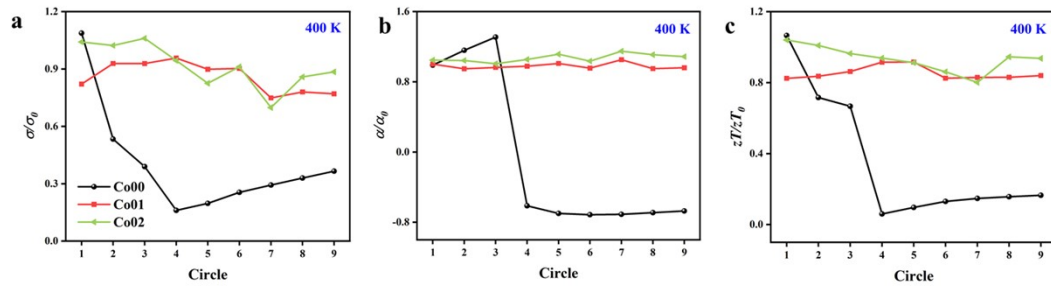
Fig. S15 | Stability performance of xCo/Mg$_{3.2}$Bi$_{1.49}$Sb$_{0.5}$Te$_{0.01}$ (x = 0, 0.01 and 0.02) at 400 K. (a) σ/σ_0, **(b)** α/α_0 and **(c)** zT/zT_0. σ_0, α_0 and zT_0 are the corresponding values before the stability measurement.
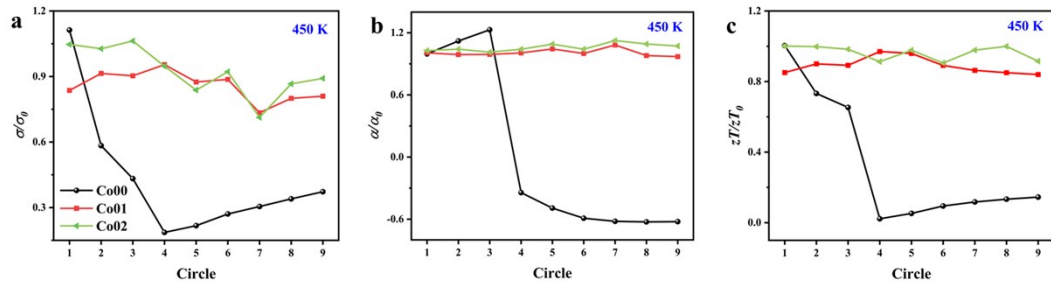
Fig. S16 | Stability performance of xCo/Mg$_{3.2}$Bi$_{1.49}$Sb$_{0.5}$Te$_{0.01}$ (x = 0, 0.01 and 0.02) at 450 K. (a) σ/σ_0, **(b)** α/α_0 and **(c)** zT/zT_0. σ_0, α_0 and zT_0 are the corresponding values before the stability measurement.

S17. Electron backscatter diffraction (EBSD) crystal-orientation maps

No significant grain size difference can be observed after the Co incorporation.
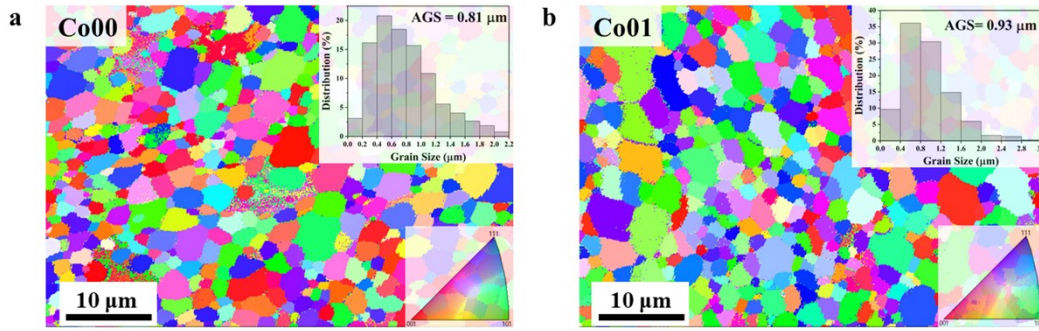
Fig. S17 | Electron backscatter diffraction (EBSD) crystal-orientation maps of x**Co/Mg**$_{3.2}$**Bi**$_{1.49}$**Sb**$_{0.5}$**Te**$_{0.01}$ **(**x **= 0 and 0.01). (a)** Co00 **and (b)** Co01.

Table S5. Density and relative density of Samples

The sample density (ρ) of xCo/Mg$_{3.2}$Bi$_{1.49}$Sb$_{0.5}$Te$_{0.01}$ (x = 0, 0.005, 0.01, 0.02, 0.03 and 0.04) measured by Archimedes method. Theoretical density is between 5.4 ~ 5.5 g/cm^3, relative density all excess 95 % of the theoretical values.

Samples	Density (g/cm^3)	Relative density (%)
Co00	5.22	95.78
Co005	5.32	97.61
Co01	5.31	97.43
Co02	5.26	96.51
Co03	5.28	96.88
Co04	5.33	97.80

References

[1] J. Yang, G. P. Meisner and L. Chen, *Applied Physics Letters*, 2004, **85**, 1140-1142.

[2] J. Zhang, L. Song and B. B. Iversen, *npj Computational Materials*, 2019, **5**, 76.

[3] M. Giehler, M. Ramsteiner, P. Waltereit, O. Brandt, K. H. Ploog and H. Obloh,

Journal of Applied Physics, 2001, **89**, 3634-3641.

[4] L. Bergman, D. Alexson, P. L. Murphy, R. J. Nemanich, M. Dutta, M. A. Stroscio, C. Balkas, H. Shin and R. F. Davis, *Physical Review B*, 1999, **59**, 12977-12982.

[5] Y. Wu, Z. Chen, P. Nan, F. Xiong, S. Lin, X. Zhang, Y. Chen, L. Chen, B. Ge and Y. Pei, *Joule*, 2019, **3**, 1276-1288.

[6] W. Peng, G. Petretto, G.-M. Rignanese, G. Hautier and A. Zevalkink, *Joule*, 2018, **2**, 1879-1893.

[7] R. Cheng, X. Shen, S. Klotz, Z. Zeng, Z. Li, A. Ivanov, Y. Xiao, L.-D. Zhao, F. Weber and Y. Chen, *Physical Review B*, 2023, **108**, 104306.

[8] R. Wang, S. Luo, X. Mo, H. Liu, T. Liu, X. Lei, Q. Zhang, J. Zhang and L. Huang, *Advanced Sustainable Systems*, 2023, **7**, 2300234.

[9] T. Zhu, Y. Liu, C. Fu, J. P. Heremans, J. G. Snyder and X. Zhao, *Advanced Materials*, 2017, **29**, 1605884.

[10] Y. C. Dou, X. Y. Qin, D. Li, L. L. Li, T. H. Zou and Q. Q. Wang, *Journal of Applied Physics*, 2013, **114**, 044906.

[11] T. Zou, X. Qin, Y. Zhang, X. Li, Z. Zeng, D. Li, J. Zhang, H. Xin, W. Xie and A. Weidenkaff, *Scientific Reports*, 2015, **5**, 17803.

[12] T. Hong, C. Guo, D. Wang, B. Qin, C. Chang, X. Gao and L.-D. Zhao, *Materials Today Energy*, 2022, **25**, 100985.

[13] X. Li, C. Chen, L. Yin, X. Wang, J. Mao, F. Cao and Q. Zhang, *Energy & Environmental Science*, 2023, **16**, 6147-6154.

[14] Z. Liu, N. Sato, W. Gao, K. Yubuta, N. Kawamoto, M. Mitome, K. Kurashima, Y. Owada, K. Nagase, C.-H. Lee, J. Yi, K. Tsuchiya and T. Mori, *Joule*, 2021, **5**.

[15] F. Zhang, C. Chen, H. Yao, F. Bai, L. Yin, X. Li, S. Li, W. Xue, Y. Wang, F. Cao, X. Liu, J. Sui and Q. Zhang, *Advanced Functional Materials*, 2020, **30**, 1906143.

[16] J.-W. Li, Z. Han, J. Yu, H.-L. Zhuang, H. Hu, B. Su, H. Li, Y. Jiang, L. Chen, W. Liu, Q. Zheng and J.-F. Li, *Nature Communications*, 2023, **14**, 7428.

[17] C. L. Condron, S. M. Kauzlarich, F. Gascoin and G. J. Snyder, *Journal of Solid State Chemistry*, 2006, **179**, 2252-2257.

[18] M. Wood, K. Imasato, S. Anand, J. Yang and G. J. Snyder, *Journal of Materials*

Chemistry A, 2020, **8**, 2033-2038.

[19] Z. Li, C. Sun, X. Li, X. Ye, K. Yang, X. Nie, W. Zhao and Q. Zhang, *ACS Applied Materials & Interfaces*, 2023, **15**, 23447-23456.

[20] L. R. Jørgensen, J. Zhang, C. B. Zeuthen and B. B. Iversen, *Journal of Materials Chemistry A*, 2018, **6**, 17171-17176.

[21] C. Xu, Z. Liang, H. Shang, D. Wang, H. Wang, F. Ding, J. Mao and Z. Ren, *Materials Today Physics*, 2021, **17**, 100336.